ACCSCIENCE PUBLISHING

Journal of Seismic Exploration

ARTICLE

Full-azimuth reflection tomography and full-waveform inversion for Permian igneous rock velocity characterization in the Tarim Basin

Peng Qi[1,2], Yu Sun[3], Zhangqing Sun[1]*, Songlin Yang[4], Jun Ning[5], Bin Hu[1], Fangchao Yan[3], Fengfan Huyan[6], Mingchen Liu[1], and Jiashun Yao[2]

[1]State Key Laboratory of Deep Earth Exploration and Imaging, College of GeoExploration Science and Technology, Jilin University, Changchun, Jilin, China

[2]Sinopec Geophysical Research Institute, Nanjing, Jiangsu, China

[3]CNNC Geological Exploration Group Co., Ltd., Beijing, China

[4]Research Institute of Exploration and Development, Liaohe Oilfield Branch Company, PetroChina, Panjin, Liaoning, China

[5]Geologic Party No. 243, China National Nuclear Corporation, Chifeng, Inner Mongolia, China

[6]Department of Earth Sciences, Faculty of Mathematical & Physical Sciences, University College London, London, United Kingdom

***Corresponding author:**
Zhangqing Sun
(sun_zhangq@jlu.edu.cn)

Citation: Qi P, Sun Y, Sun Z, *et al*. Full-azimuth reflection tomography and full-waveform inversion for Permian igneous rock velocity characterization in the Tarim Basin. *J Seismic Explor*. doi: 10.36922/JSE026340157

Received: August 21, 2026

Revised: September 4, 2026

Accepted: September 7, 2026

Published online: September 23, 2026

Copyright: © 2026 Author(s). This is an Open-Access article distributed under the terms of the Creative Commons Attribution License, permitting distribution, and reproduction in any medium, provided the original work is properly cited.

Publisher's Note: AccScience Publishing remains neutral with regard to jurisdictional claims in published maps and institutional affiliations.

Abstract

In Northwest China, igneous rocks are widely developed within the Permian strata. Their high velocities and rapid lateral variations degrade the imaging of the underlying strata, producing structural distortions and weakened reflections that can be misinterpreted as faults or low-relief structures. Moreover, conventional model building struggles to recover their velocity field. To address this challenge, we present a two-step velocity-model-building workflow that combines offset vector tile (OVT) domain reflection tomography with full-waveform inversion (FWI) to characterize the Permian igneous rocks. In the first step, after five-dimensional data regularization and OVT sorting, full-azimuth OVT-domain reflection tomography was used to build the velocity model, constraining lateral velocity variations in the igneous interval that conventional offset-domain tomography leaves unconstrained. This yields an initial model accurate enough for the subsequent inversion. In the second step, FWI with an edge-preserving total-variation regularization was applied. The regularization retains the blocky boundaries of the igneous body in place of structure-oriented smoothing, and the inversion successfully characterizes the velocity structure of the Permian igneous rocks. The effectiveness of the inversion is demonstrated by comparisons of common-image-point gathers, well velocities, and pre-stack depth migration images. The workflow provides a practicable route to velocity modeling and imaging in land igneous-rock settings.

Keywords: Full-waveform inversion; Offset vector tile; Reflection tomography; Velocity model building; Igneous rocks; Tarim Basin

1. Introduction

Permian igneous rocks are widely developed in the sedimentary basins of northwest China. Characterized by high velocities, strong internal heterogeneity, and blocky, irregular boundaries, these bodies are difficult to resolve with conventional velocity modeling and severely distort the seismic response of the underlying strata. Forward modeling in this region shows that inaccurate igneous velocity and geometry produce imaging pull-up, weakened sub-igneous reflections, and chaotic diffraction zones easily misinterpreted as faults or fracture corridors,[1] a misinterpretation confirmed by drilling.[2] Furthermore, even moderate smoothing of the igneous velocity field generates spurious faults and false low-relief structures below the body.[3,4] The accuracy of the igneous velocity model therefore directly governs sub-igneous imaging quality.

Conventional velocity modeling in igneous provinces faces intrinsic limitations. Ray-based reflection tomography suffers from illumination shadows beneath high-velocity bodies: the strong impedance contrast reflects most of the incident energy, producing quasi-total reflection in ray tracing and leaving the interior and flanks of the body poorly constrained.[5] The difficulty is compounded by the rapid lateral variation of igneous velocities, which smooth, long-wavelength conventional tomographic updates cannot adequately track. Interpretation-constrained tomography, which feeds horizon and attribute interpretation back into the tomographic update, has proven effective in suppressing igneous-induced artifacts.[2] Its accuracy, however, is governed by the reliability of the prior geological information and the accuracy of horizon picking. Compared with common-offset tomography, full-azimuth tomography in the offset vector tile (OVT) domain[6] can delineate small-scale velocity variations in finer detail.[7] It inverts the residual moveout as a function of both offset and azimuth, and the azimuthal variations left unused by common-offset analysis thus provide additional constraints on laterally varying velocity fields. However, such methods are constrained on land by the irregular acquisition geometry. The single-fold content of each OVT gather also leaves the signal-to-noise ratio low, which hampers the tomographic inversion.

Full-waveform inversion (FWI) is generally considered the most accurate velocity modeling method available at present, since it exploits the kinematic as well as the dynamic content of the recorded wavefield.[8,9] Its application to land data, however, remains demanding: limited low-frequency content, strong near-surface complexity, and a strong dependence on initial-model accuracy aggravate the nonlinearity of the inversion and increase the risk of cycle skipping,[3,10] motivating continued development of cycle-skipping-resistant misfit functions.[11,12] Land applications have nonetheless received growing attention in recent years.[13] Cui *et al*.[3] combined refraction-waveform inversion of the shallow section with reflection FWI of the deeper section, and imaged the deep carbonate reservoirs beneath the igneous rocks of the Tarim Basin. Hu *et al.*[14] applied reflection FWI under structural constraints to land data from northwest China, characterizing the velocity of deep weathering crusts and improving the imaging of the reservoirs beneath them. In these applications, the velocity model serves as a target in the deep section. Igneous bodies lying above such targets, whose velocity changes rapidly over short distances and which themselves distort the underlying image, have rarely been treated as the object of characterization.

In this study, we present a practical two-step velocity-model-building workflow, combining OVT-domain reflection tomography with FWI, to characterize an igneous complex in a land survey. The first step yields the initial model that the inversion requires. Five-dimensional (5D) data regularization and OVT sorting deliver regularized, azimuth-preserving gathers with an improved signal-to-noise ratio. Full-azimuth tomography then uses these gathers to constrain lateral velocity variation around the igneous body that a common-offset workflow leaves unresolved. The resulting model is benchmarked against a conventional tomography within the same framework.

The tomography step thus supplies the initial model from which the subsequent FWI recovers the velocity of the igneous body. The strong surface waves in the land records are muted from the input shot gathers to avoid contaminating the inversion. A classical least-squares FWI is then applied in a single stage without wave-type separation, enabled by the accuracy of the OVT-derived initial model. Multiscale frequency continuation[15] mitigates the nonlinearity of the inversion. An edge-preserving regularization[16,17] is imposed to retain the blocky boundaries of the igneous body. Quality control (QC) includes interleaved shot-gather QC, common image point (CIP) gather QC, well-velocity QC, and pre-stack depth migration (PSDM) QC. By applying this workflow to a land dataset in Northwest China, we obtained a more accurate velocity model of the Permian igneous rocks, removed structural distortions in the underlying strata, and provided a practical reference for other igneous provinces.

2. Methods

In this study, we applied our velocity-model-building workflow to a three-dimensional land survey in the Tarim Basin, Northwest China. The main acquisition parameters

of the survey are summarized in Table 1. The survey area features simple surface conditions with small elevation variation, and its shallow-to-middle section consists mainly of near-horizontal, layered strata. Beneath this otherwise simple overburden, however, lies a Permian igneous complex (Figure 1) that makes velocity model building difficult and degrades the image of the underlying strata. On an amplitude slice through the igneous interval (Figure 1A), the smooth, high-amplitude response on the left gives way, across a sharp sinuous boundary, to a chaotic, short-wavelength response on the right that is characteristic of igneous rocks. On a representative time-migrated section (Figure 1B), the reflectors below approximately 3 s exhibit pronounced structural undulations where they cross this boundary, consistent with the strong lateral velocity contrast introduced by the igneous body.

The workflow adopted in this study is summarized in Figure 2, from the statics-corrected shot gathers to the final velocity model. Common-offset tomography constrains the lateral velocity variation of the igneous interval only weakly. The velocity model was therefore first built in the OVT domain, where the offset and azimuth of every trace are preserved. 5D data regularization preceded this step so the OVT gathers were usable for tomography. The resulting model then served as the starting point for a classical least-squares FWI, in which edge-preserving regularization retained the boundaries of the igneous body sharp.

Table 1. Acquisition parameters of the three-dimensional land survey

Parameter	Value
Source type	Dynamite
Source point interval	50 m
Source line interval	300 m
Receiver point interval	50 m
Receiver line interval	300 m
Receiver patch	36 lines × 264 channels
Bin size	25 m × 25 m
Nominal fold	396 (22 in-line × 18 cross-line)
Maximum in-line offset	6,575 m
Maximum cross-line offset	5,375 m
Maximum offset	8,492 m
Aspect ratio (cross-line to in-line)	0.817
Full-fold area	548.82 km²

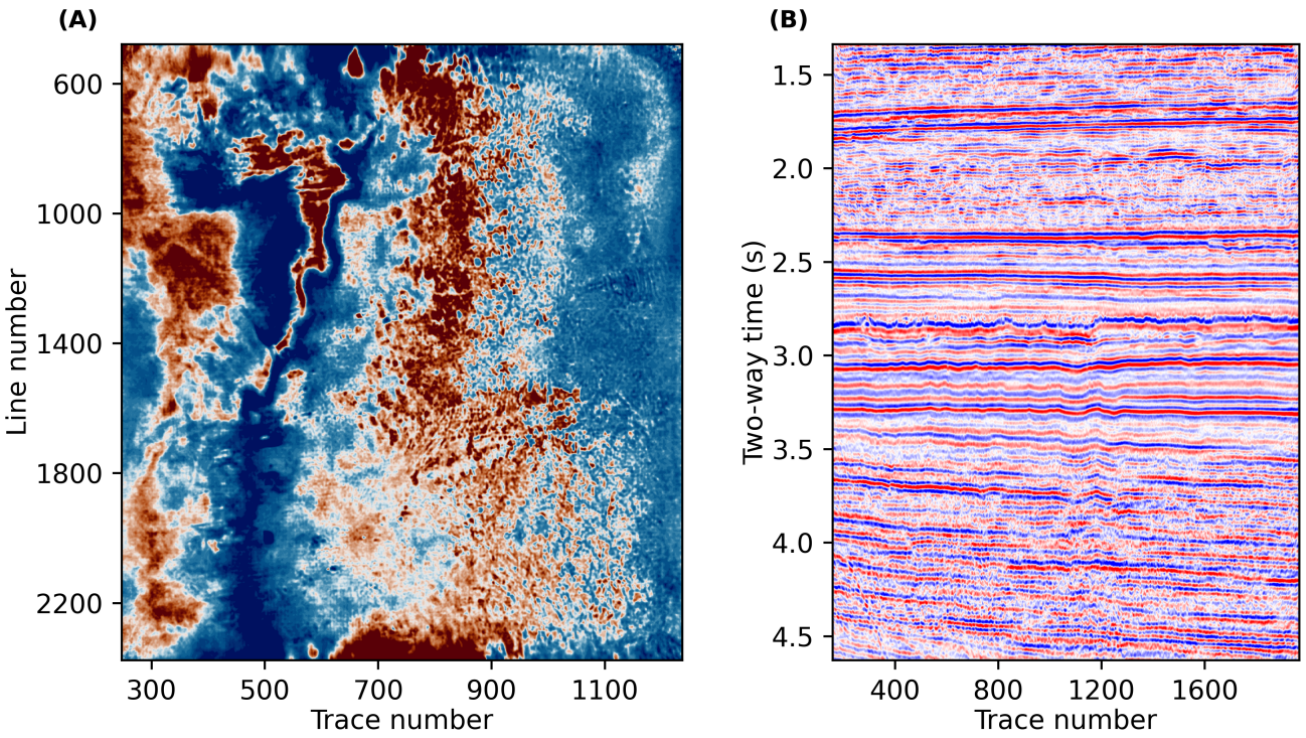


Figure 1. Igneous rocks in the study area. (A) Amplitude slice through the Permian igneous interval at a two-way time of 2.8 s from the pre-stack time migration (PSTM) volume. (B) Representative PSTM section across the igneous complex.

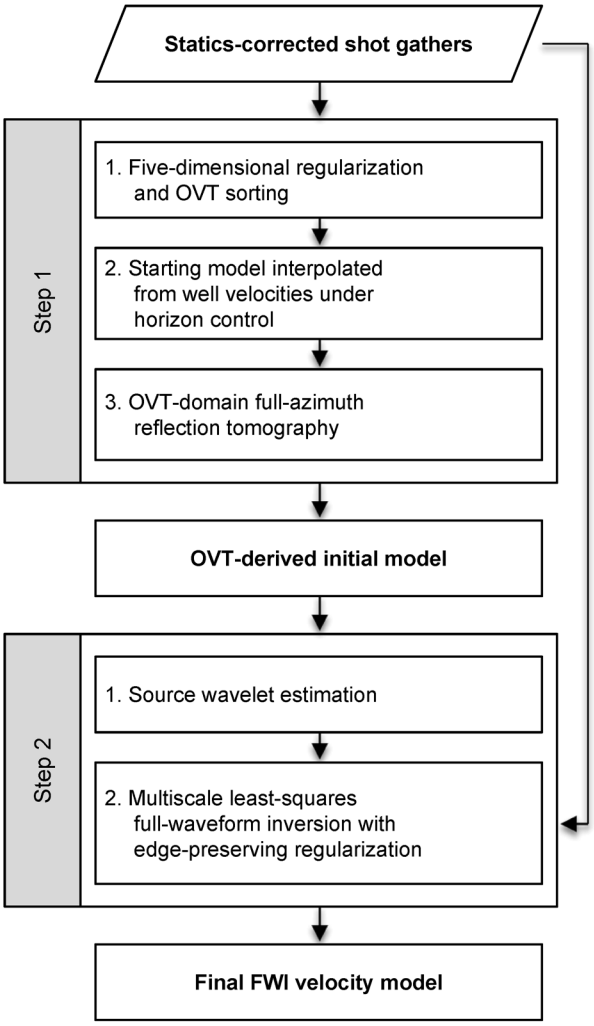


Figure 2. Two-step velocity model building workflow
Abbreviations: FWI: Full-waveform inversion; OVT: Offset vector tile.

2.1. Five-dimensional data regularization

Full-azimuth velocity model building in the OVT domain succeeds only where the OVT gathers sample each subsurface bin uniformly in offset and azimuth. Land acquisition, however, is often constrained by surface obstacles and operational limitations, which leave the source-receiver geometry irregular and the signal-to-noise ratio relatively low. To make the OVT gathers more uniform in offset and azimuth and to raise their signal-to-noise ratio, 5D data regularization was performed prior to OVT-domain velocity model building.

Multidimensional seismic data regularization has been approached in the Fourier domain by minimum weighted-norm interpolation[18] and by the anti-leakage Fourier transform,[19] among other schemes. In this study, we applied matching pursuit Fourier interpolation,[20,21] which reconstructs the recorded wavefield in 5D (inline, crossline, offset, azimuth, and time) by iteratively selecting its dominant Fourier components. Specifically, the reconstruction minimizes the objective function (**Equation 1**):

$$J(\mathrm{x}) = \left\| \mathrm{d} - \Gamma \mathrm{F} \mathrm{x} \right\|_2^2 \quad (1)$$

where d denotes the irregularly sampled input data, x is the vector of Fourier coefficients to be estimated, F is the 5D Fourier synthesis operator, and Γ is the sampling operator that maps the synthesized wavefield onto the actual acquired trace locations. **Equation 1** was solved using a greedy approach. At each iteration, the most energetic Fourier component was identified using anti-aliasing priors derived from the unaliased low-frequency part of the spectrum and subtracted from the residual. Retaining only coherent spectral components, matching pursuit Fourier interpolation interpolated the data onto a regular grid, attenuated random noise, and remained robust where acquisition gaps were large. After regularization, the data were sorted into OVTs,[6] each of which is a single-fold subset of a cross-spread with a limited spread in offset and azimuth, so that both are preserved through pre-stack depth migration.

Figure 3 shows the source point distribution and the common midpoint gathers before and after 5D regularization. The source points became more regularly distributed across the survey, while the events in the common midpoint gathers became more continuous and had a higher signal-to-noise ratio. Figure 4 displays the offset and azimuth attributes of the OVT tiles within a representative cross-spread; each tile spans a narrow and nearly constant range of both. Together, the tiles cover the offset-azimuth plane without overlap or gaps.

2.2. Initial model building with offset vector tile-domain reflection tomography

Full-waveform inversion can refine a velocity model only within the convergence basin of the starting model. If the long-wavelength background velocity is in error, simulated events may shift by more than half a cycle relative to the observed ones, and the inversion converges to a cycle-skipped local minimum.[22] This requirement is particularly demanding in the presence of the igneous complex, whose strong and short-wavelength lateral velocity variations are precisely the components that conventional model building struggles to recover. Conventional reflection tomography is performed on common-offset CIP gathers, in which

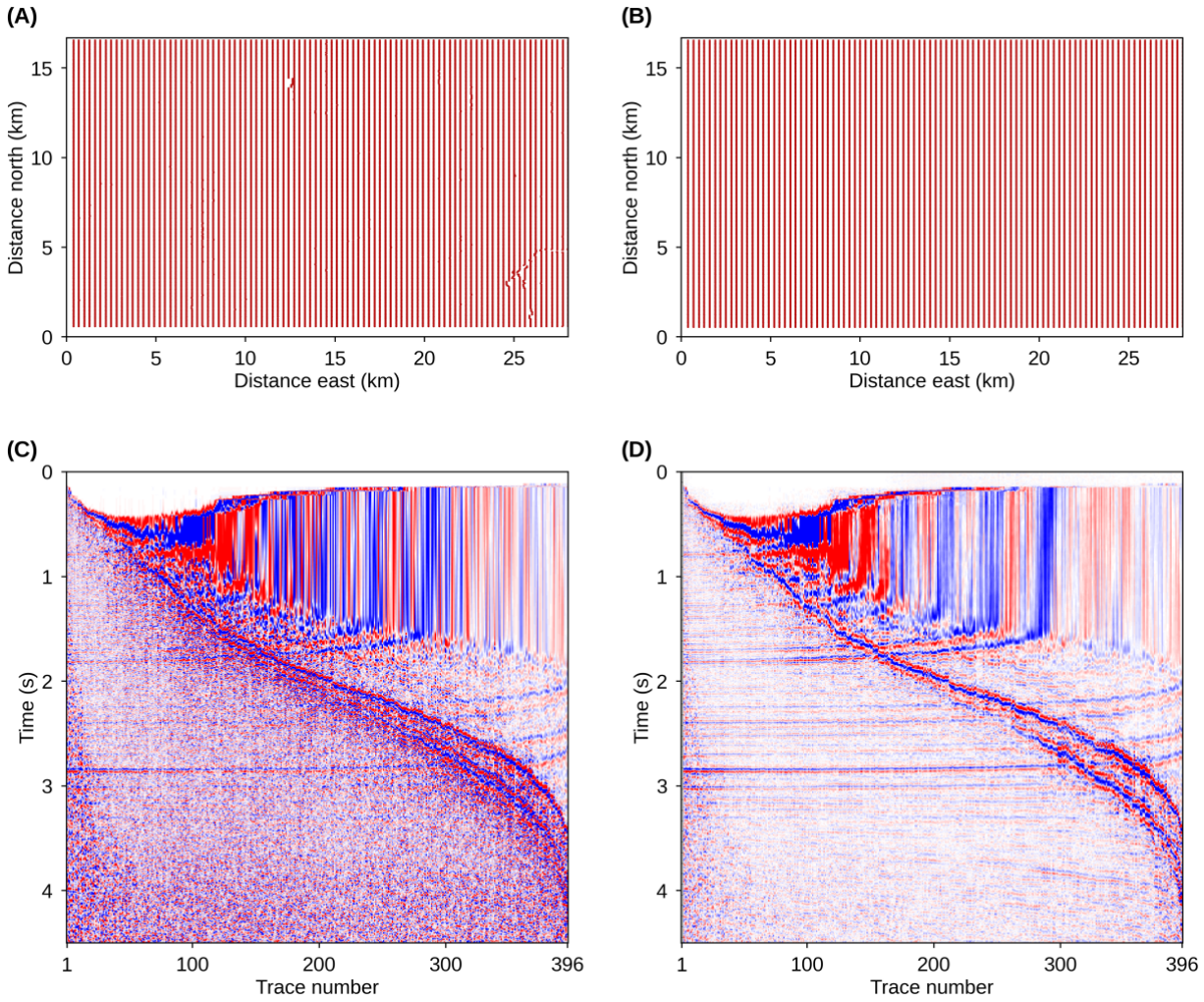


Figure 3. Comparison before and after five-dimensional regularization. Source point distribution (A) before and (B) after regularization. Common midpoint gathers (C) before and (D) after regularization.

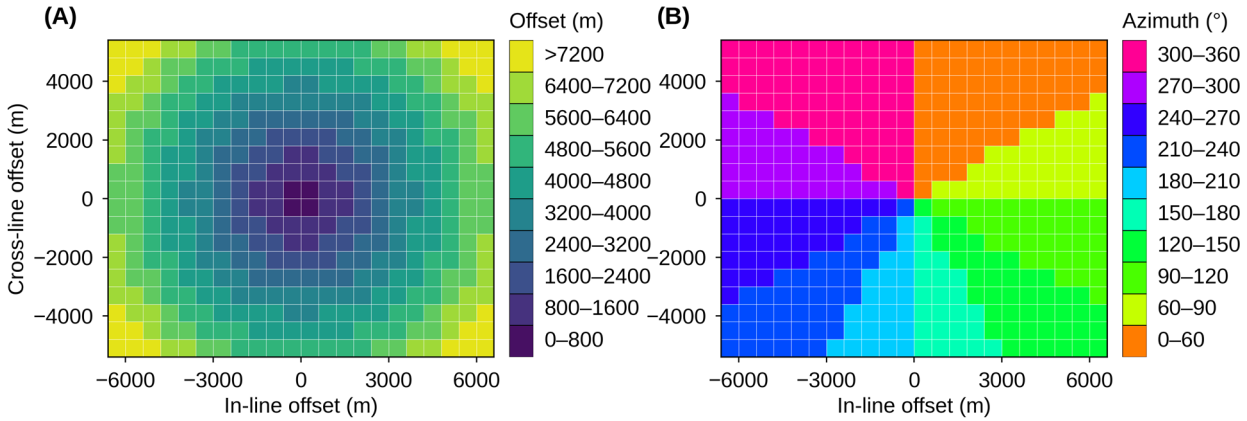


Figure 4. Offset and azimuth attributes of the offset vector tiles (OVTs) within a representative cross-spread after regularization. (A) Offset distribution. (B) Azimuth distribution.

migration loses azimuthal information, so the inversion resolves only relatively large-scale velocity variations.[7] Such a model provides little of the detail required over the igneous interval.

We therefore performed reflection tomography in the OVT domain, so that the resulting initial model would be accurate enough for the inversion that follows.[7] The tomography started from a velocity model obtained by smooth interpolation of well velocities under horizon control. OVT-domain pre-stack depth migration then delivered full-azimuth CIP gathers that preserve both offset and azimuth. Figure 5A and 5B shows CIP gathers migrated with this starting model in the two domains. The full-azimuth gathers revealed clear azimuth-dependent residual moveout near the igneous body. Such moveout is invisible to the conventional workflow and therefore cannot be corrected by it. Residual moveout was picked automatically on these three-dimensional gathers, and the ray-tracing and tomographic equations for all azimuths were then solved jointly for the velocity under the isotropic acoustic approximation. After the OVT-domain update, the azimuth-dependent moveout is substantially reduced (Figure 5C). For comparison, we ran conventional common-offset tomography within the same framework, differing only in the gather domain used for residual-moveout picking. Figure 6 shows the two tomographic models over the igneous interval. The OVT-domain model reproduced the lateral velocity variation of the igneous body in greater detail, whereas the conventional model recovered mainly the large-scale background trend. This OVT-domain model was adopted as the initial model for the multiscale FWI. It provides the long-wavelength background, while the inversion itself resolves the sharp boundaries of the igneous body.

2.3. Full-waveform inversion with edge-preserving regularization

Full-waveform inversion recovers the velocity model by iteratively reducing the misfit between observed and simulated data.[8,23] Each iteration consisted of four steps: the wave equation was solved in the current model to generate the simulated wavefields,[14] the data residual was formed into an objective function, the adjoint-state method yielded its gradient, and the model was updated accordingly. The cycle was repeated until convergence. We adopted the conventional least-squares waveform objective function (**Equation 2**):

$$J_{\mathrm{LS}}(\mathrm{m}) = \frac{1}{2}\sum_{s}\sum_{r}\int \left| u(\mathrm{x}_r, t; \mathrm{m}) - d(\mathrm{x}_r, t) \right|^2 \mathrm{d}t \tag{2}$$

where m denotes the velocity model, and d and u are the data observed and simulated for source s and receiver r.[8] The complete recorded wavefield, transmitted and reflected energy alike, enters **Equation 2** in a single inversion stage, so that the gradient remains the standard adjoint-state full-wavefield kernel. An objective function of this form demands an initial model that already lies close to the true long-wavelength velocity structure. The OVT-derived full-azimuth tomographic model meets this requirement, since the events simulated in it are already well aligned with the observed records.

Gradient conditioning, by contrast, must be adapted to the target geometry. Structure-oriented smoothing,

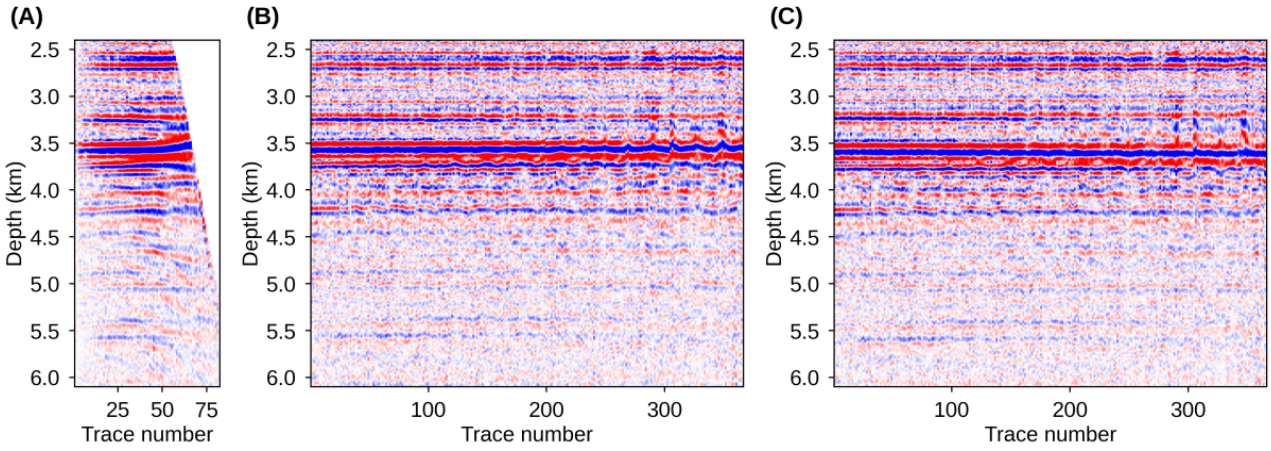


Figure 5. Comparison of the common image point (CIP) gathers. (A) Conventional common-offset gather and (B) full-azimuth gather, both migrated with the starting velocity model. (C) Full-azimuth gather migrated with the final offset vector tile (OVT) domain tomographic model.

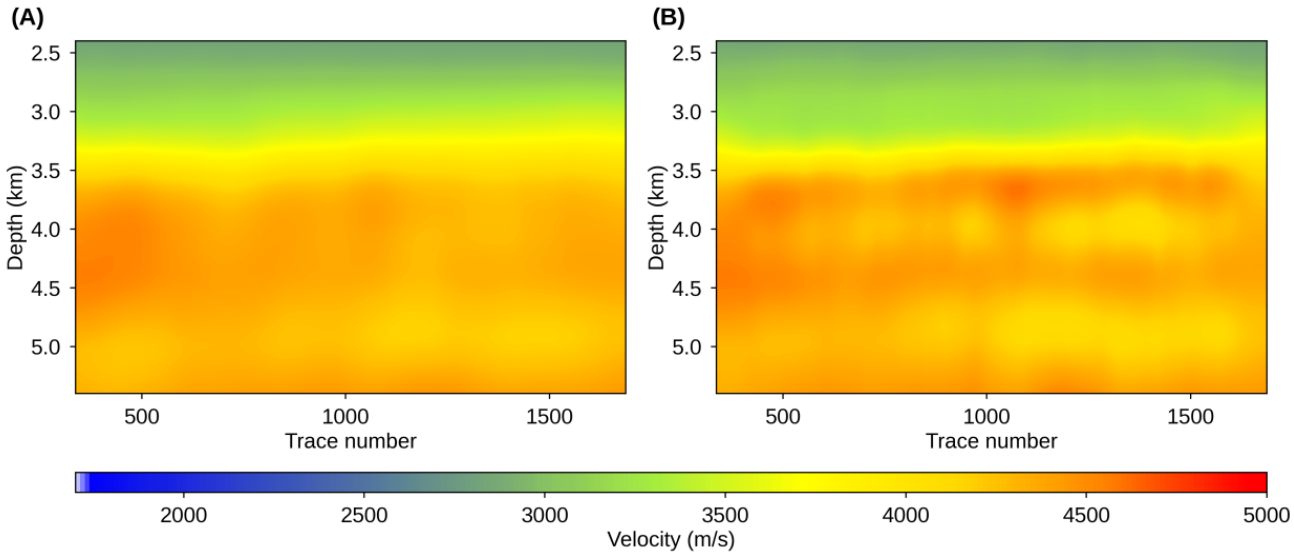


Figure 6. Comparison of the velocity models. (A) Conventional common-offset reflection tomography. (B) Full-azimuth reflection tomography in the offset vector tile (OVT) domain.

effective for layered targets,[14] would smear the blocky, discordant boundaries of the igneous body if applied here. Instead, an edge-preserving anisotropic total-variation term was appended to the objective function[16,17]:

$$J(\mathrm{m}) = J_{\mathrm{LS}}(\mathrm{m}) + \varepsilon\left(\left\|\mathrm{D}_x\,\mathrm{m}\right\|_1 + \left\|\mathrm{D}_z\,\mathrm{m}\right\|_1\right) \tag{3}$$

where D_x and D_z denote the horizontal and vertical gradient operators, $\|\cdot\|_1$ is the ℓ_1 norm, and ε is the trade-off parameter. Penalizing the ℓ_1 norm of the model derivatives in both directions promotes internal homogeneity of the high-velocity body while keeping its boundaries sharp. The ℓ_1 term was not differentiable where a model derivative vanishes, so its gradient contribution was evaluated as a subgradient, with the sign taken as zero at that point. Rather than being assigned directly, ε was obtained from a dimensionless ratio between the data misfit and the regularization term, both evaluated in the initial model.[16]

Consistent with this scheme, the inversion operates directly on the statics-corrected, unregularized shot gathers, retaining the full record length and muting surface waves. These records retain usable low-frequency signal, which sets the lowest band used in the inversion.[10] In addition, the maximum offset of approximately 8.5 km is large relative to the target burial depth of approximately 3.5 km, so that the igneous interval was sampled over a wide range of reflection angles and constrained at long offsets. The nonlinearity of the inverse problem was mitigated further by proceeding as a multiscale continuation from low to high frequency bands, with adequate wavenumber overlap between neighboring bands.[15,24] The source wavelet was estimated with a shaping-operator approach. We extracted an initial wavelet from the field data and then applied the operator, derived by matching simulated near-offset traces to the corresponding observed traces.[25]

Regarding the wave equation used in the modeling, the igneous interval forms a strong impedance contrast with the surrounding strata, and elastic waveform inversion offers advantages in this setting. It reproduces the mode conversions generated at the top and base of the interval and describes the reflection amplitudes that these contrasts control. Researchers have applied this type of inversion to land data sets in recent years.[13] An acoustic wavefield carries no shear energy, so the amplitude signature of these conversions enters the data residual.[5] Part of that residual is then absorbed by the least-squares objective as a velocity perturbation. The survey here, however, recorded a single vertical component and carried no information on shear velocity. An elastic inversion also couples several parameters in a single update, increasing the inverse problem's nonlinearity and raising computational cost.[9] To establish a more practical workflow, the wavefield was modeled under the isotropic acoustic approximation. The total-variation prior on the model side then enforced sharp igneous boundaries rather than relying on data amplitudes.

3. Results and discussion

The inversion was carried out in three frequency bands, with high-cut frequencies of 3, 4, and 5 Hz. We performed six iterations within each band before proceeding to the next. The parameters of the inversion are summarized in Table 2. Figure 7 presents the shot-gather QC for this configuration. Figure 7A shows the observed record for a representative receiver line, Figure 7B shows the record simulated in the OVT-derived initial model, and Figure 7C shows the record simulated in the final FWI model. Figure 7D and 7E interleaves the observed traces with these two simulated records. In Figure 7D, the events simulated in the OVT-derived initial model are already well aligned with the observed traces, which confirms the adequacy of that model as a starting point for the inversion. After the multiscale inversion (Figure 7E), the alignment improved further, and the interleaved events became more continuous and coherent over the displayed window.

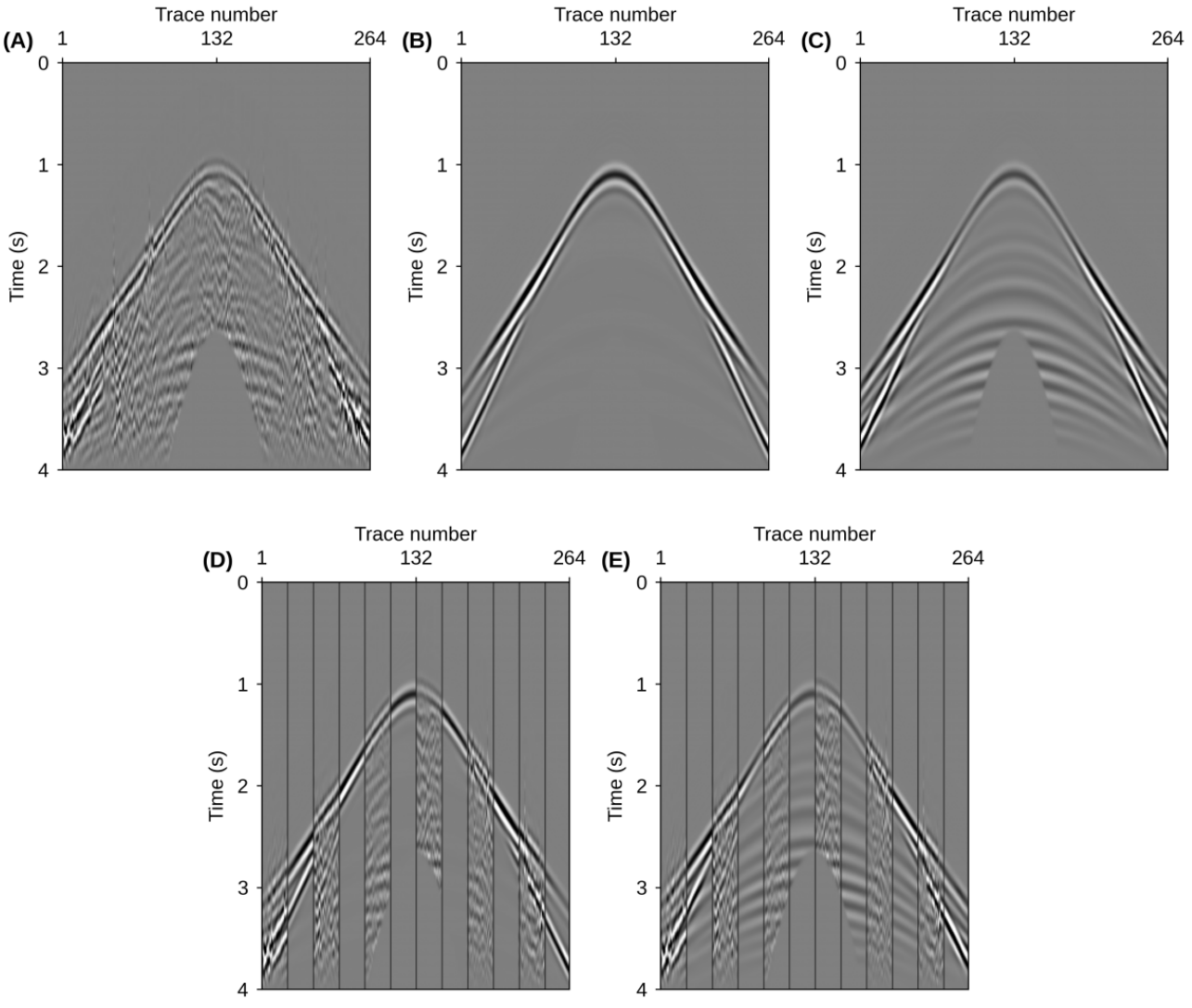


Figure 7. Shot-gather quality control. (A) Observed record. (B) Record simulated before full-waveform inversion (FWI). (C) Record simulated after FWI. (D) Observed data interleaved with (B). (E) Observed data interleaved with (C).

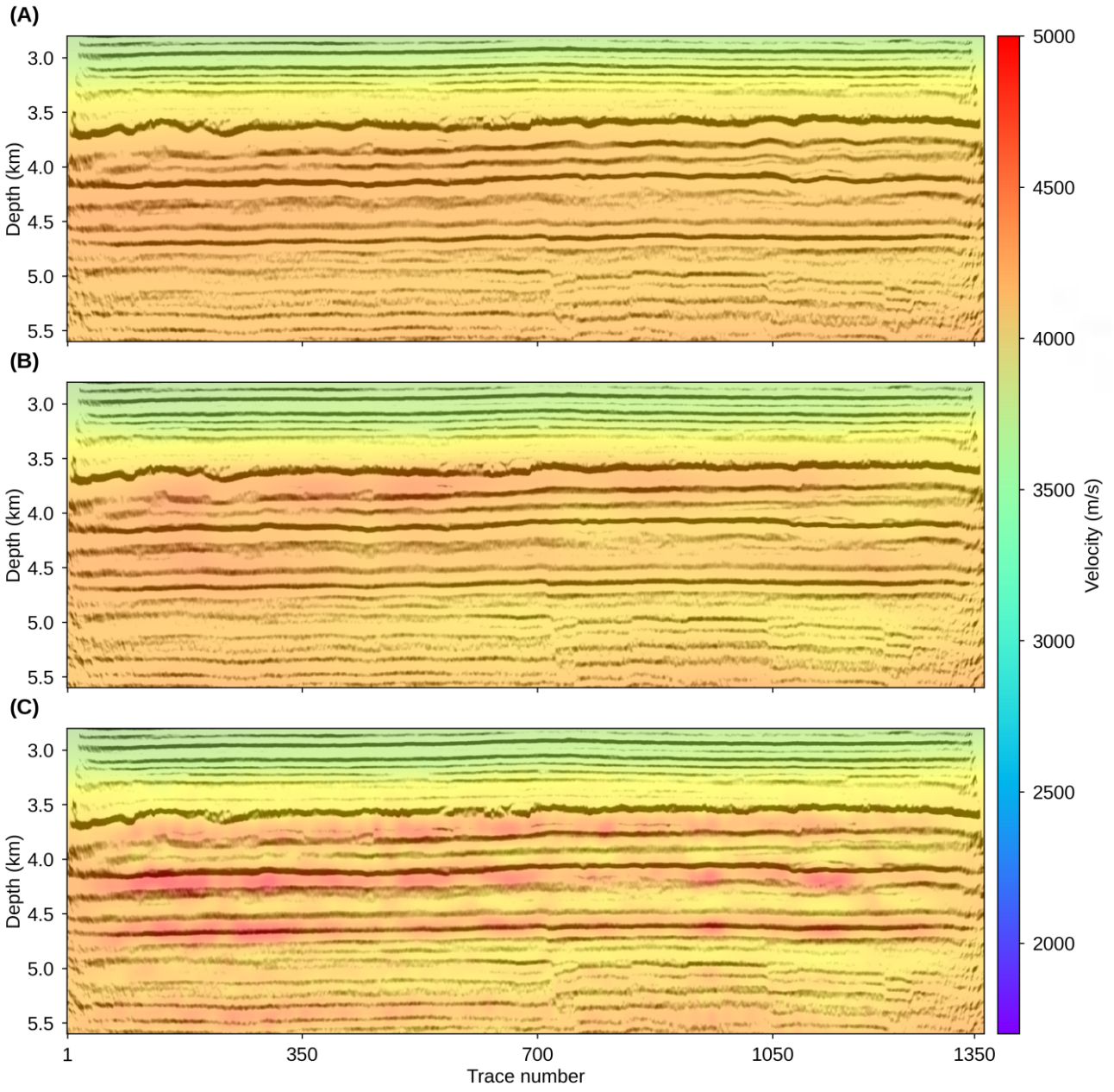


Figure 8. Comparison of the velocity model, each overlaid with the corresponding pre-stack depth migration (PSDM) stacked section. (A) Interpolated starting model. (B) Offset vector tile (OVT) domain tomographic model. (C) Final full-waveform inversion (FWI) model.

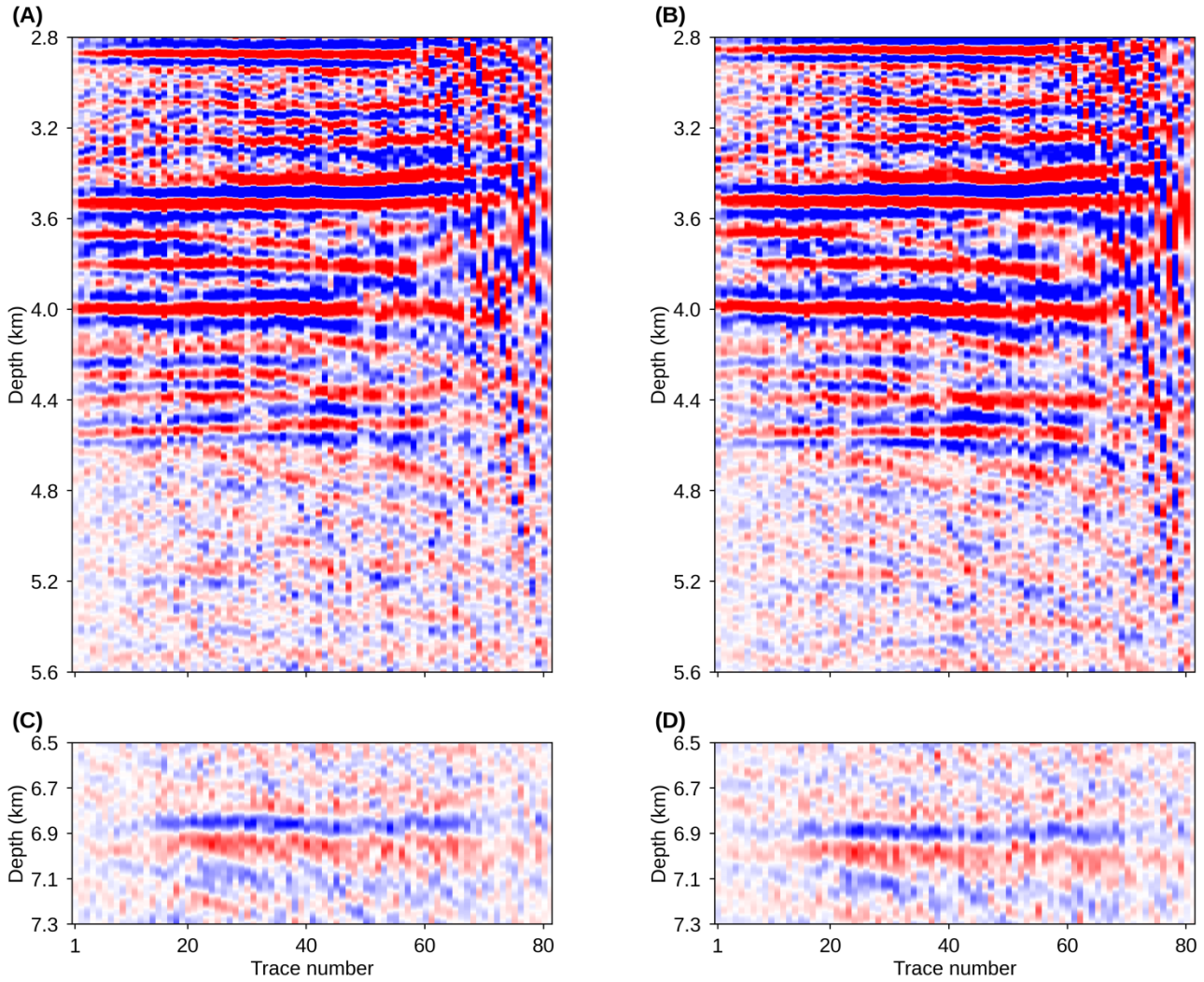


Figure 9. Comparison of the common-offset common image point (CIP) gathers. (A, C) Migrated with the offset vector tile (OVT)-derived initial model. (B, D) Migrated with the final full-waveform inversion (FWI) model.

The velocity model was tracked through the workflow. Figure 8 shows the interpolated starting model (Figure 8A), the OVT-domain tomographic model (Figure 8B), and the final FWI model (Figure 8C) along a representative section crossing the igneous complex, each of them overlaid on the corresponding migrated section. As the workflow progressed, the velocity model became progressively more detailed, and its structure agreed increasingly well with the subsurface image. The starting model reproduced only the background trend of the high-velocity interval, which appears as a single band of nearly uniform velocity, and the tomographic model added a large-scale lateral gradient to that band while leaving it internally smooth. In the final FWI model, the interval instead consisted of discrete high-velocity patches of limited lateral extent, separated by zones of lower velocity, and the anisotropic total-variation term kept the boundaries between these patches sharp. The top and base of the interval coincided with the reflectors imaged in the migrated section, whereas in the two preceding models, they fell within a gradational transition that has no counterpart in the image.

Gather flatness provides an image-domain check on the velocity update. Figure 9 compares CIP gathers generated with the initial model against those generated with the final FWI model. With the initial model, the reflections beneath the igneous interval remain discontinuous at far offsets (Figure 9A). With the final FWI model, these far-offset events aligned better and became more continuous, and the

gathers beneath the igneous body were correspondingly flatter (Figure 9B). At greater depth, a reflection at about 6.9 km was distorted by the velocity anomaly of the igneous body and was not level across offsets with the initial model (Figure 9C). With the final FWI model, it became essentially level (Figure 9D), indicating that the FWI velocity update is effective within the igneous body itself.

Figure 10 shows the sonic velocity at a well location together with three velocity profiles. These profiles correspond to the interpolated starting model, the OVT-domain tomographic model, and the final FWI model. The starting model, constructed by interpolating well velocities under horizon control, reproduced the background trend of the section but varied smoothly across the igneous interval. The tomographic model improved background velocity accuracy, but it still lacked detail across the igneous interval. The final FWI model developed a local velocity high at the depth at which the sonic log records one. As a result, the velocity magnitude of the interval and the positions of its top and base were delineated more sharply than in the two preceding models. Away from this interval, the log varied on a finer scale than the inversion represents, and the comparison was correspondingly limited to the general trend.

Table 2. Parameters of the full-waveform inversion

Parameter	Value
Initial model	OVT-domain full-azimuth tomographic model
Wave equation	Isotropic acoustic
Forward modeling scheme	Time-domain finite difference
Grid spacing	50 m
Model dimensions	797 × 596 × 301 grid points in x, y, and z (39.8 km × 29.8 km × 15.0 km)
Time step	3 ms
Input data	Statics-corrected, unregularized shot gathers with surface waves muted
Source wavelet	Shaping-operator estimate from the field data
Objective function	Least squares (**Equation 2**)
Regularization	Anisotropic total variation (**Equation 3**)
Frequency bands (high-cut)	3, 4, and 5 Hz
Iterations per band	6

Abbreviation: OVT: Offset vector tile.

Figure 11 shows the Kirchhoff PSDM images obtained with two velocity models: the conventional common-offset tomography model and the final FWI model. In the conventional-tomography image, the reflectors beneath the igneous complex were poorly continuous and exhibited spurious structural distortions induced by the velocities of the overlying igneous rocks (Figure 11A). The comparison shows that the FWI model removes these distortions and that the underlying reflectors can be followed more consistently (Figure 11B). The change is not confined to the section immediately below the igneous rocks. For the bead-like reflection at a depth of about 9.4 km, the event was more tightly focused and laterally compact in the FWI image (Figure 11D) than in the conventional tomography image (Figure 11C). Overall, the complete two-step workflow yields a clearly improved image of the section beneath the igneous complex.

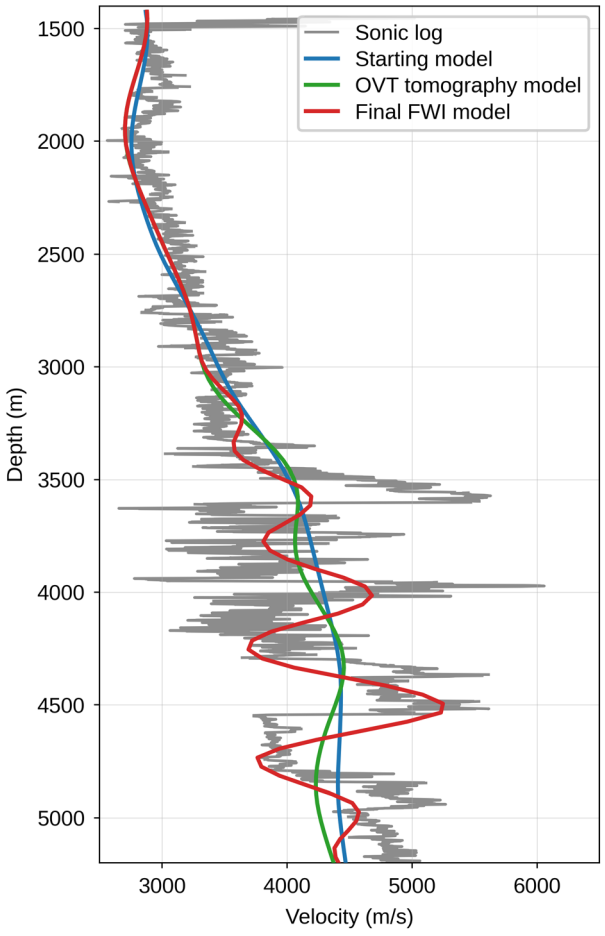


Figure 10. Comparison of the sonic log and model velocities at a well location

Abbreviations: FWI: Full-waveform inversion; OVT: Offset vector tile.

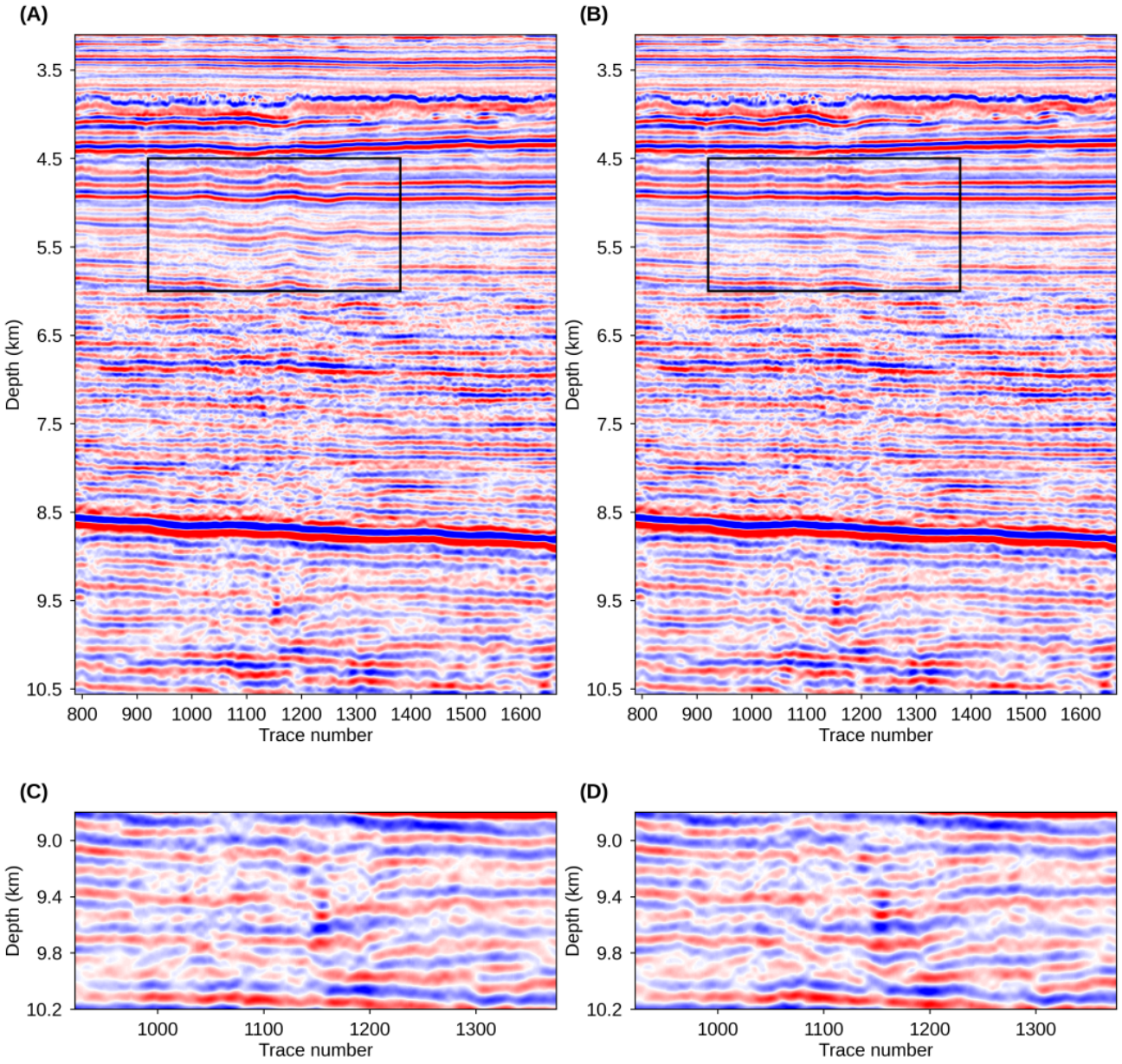


Figure 11. Kirchhoff pre-stack depth migration (PSDM) images from two velocity models. (A) Conventional-tomography velocity model. (B) Final full-waveform inversion (FWI) model. (C, D) Enlargements of (A) and (B) over the depth interval 8.8-10.2 km.

4. Conclusion

In the Tarim Basin, Northwest China, Permian igneous rocks are widespread, and the high-velocity complex they form distorts the image of the underlying strata. Although conventional tomography recovers the large-scale background trend, it leaves the lateral velocity variations of the igneous interval poorly constrained. To address this, we present a two-step workflow in which FWI refines the velocity of the igneous complex, starting from an initial model built by OVT-domain reflection tomography. The field application shows that both the velocity model and the depth image over the igneous interval are improved.

In the first step, 5D data regularization improved offset-azimuth uniformity in the OVT gathers and increased their signal-to-noise ratio. Full-azimuth reflection tomography was performed on these gathers to build the initial model.

By preserving the azimuth constraint on lateral velocity variations in the igneous interval, it recovered the body velocity in greater detail than conventional common-offset tomography.

In the second step, a classical least-squares FWI, driven by the full recorded wavefield after surface-wave muting, was applied to the initial model built in the first step. A multiscale frequency continuation was combined with an edge-preserving total-variation regularization, which refined the velocity of the igneous body while keeping its boundaries sharp. Finally, we derived a detailed velocity model of the igneous complex.

With this workflow, the depth image removes spurious structural distortions induced by inaccurate igneous velocities, and the reflectors beneath the igneous complex are followed more consistently. The bead-like reflection from the deeper target is also more tightly focused. These results indicate that the two-step workflow effectively characterizes igneous velocities in land seismic data. The workflow can therefore be extended to other land surveys in which igneous rocks impede velocity model building and imaging. Future work can explore applying elastic FWI in igneous settings to characterize the velocity of the igneous body more accurately.

Acknowledgments

None.

Funding

This work was supported by the Deep Earth Probe and Mineral Resources Exploration National Science and Technology Major Project (2025ZD1006800), the China National Nuclear Corporation Uranium Industry's "Open Competition Mechanism" Technology Research Project (No.202302), the China National Petroleum Corporation Liaohe Oilfield Branch Entrusts Technical Service Project (LHYT-KTKFYJY-2024-JS-6439), and the National Key R&D Program of China under Grants 2023YFC2906700 and IGCP-675.

Conflict of interest

The authors declare they have no competing interests.

Author contributions

Conceptualization: Peng Qi, Yu Sun, Zhangqing Sun
Formal analysis: Songlin Yang, Jun Ning, Bin Hu, Fangchao Yan
Investigation: Fengfan Huyan, Mingchen Liu
Supervision: Zhangqing Sun
Visualization: Jiashun Yao
Writing–original draft: Peng Qi, Jiashun Yao
Writing–review & editing: Peng Qi, Yu Sun, Zhangqing Sun

Availability of data

All analyzed data are presented in the paper.

References

1. Sun D, Shi X, Wang Z, *et al*. Talimu pendi Halahatang diqu Erdiexi huochengyanti dui xiafu diceng dizhen chengxiang yingxiang [The influence of Permian igneous rock on the seismic imaging of underlying strata in Hanilcatam area, Tarim Basin]. *Nat Gas Geosci*. 2018;29(12):1781-1787. [In Chinese]

   doi: 10.11764/j.issn.1672-1926.2018.10.019

2. Zhu L, Ma L, Bai Y, Cai J, Gao H. Shunbei chaoshen duankongti dizhen duo xinxi yueshu sudu jianmo [Velocity modeling of an ultra-deep fault-controlled reservoir in Shunbei area, China, using a multi-information constraint]. *Geophys Prospect Pet*. 2019;58(6):864-873. [In Chinese]

   doi: 10.3969/j.issn.1000-1441.2019.06.009

3. Cui Y, Peng G, Wu G, Shang S, Guo N, Zhao R. Quan boxing fanyan zai fengdongxing chuceng sudu jianmo zhong de yingyong [Application of full waveform inversion velocity model-building technology for the fractured-vuggy reservoir]. *Chin J Geophys*. 2016;59(7):2713-2725. [In Chinese]

   doi: 10.6038/cjg20160734

4. Jiang Z, Jiao J, Qi Q, Deng X. Quantitative elimination of seismic pseudofaults and fine analysis of true faults underlying igneous rocks of no-well areas: A case study of Shuntuoguole uplift in Tarim Basin. *Lithosphere*. 2024;2024(2). doi: 10.2113/2024/lithosphere_2023_129

5. Jones IF, Davison I. Seismic imaging in and around salt bodies. *Interpretation*. 2014;2(4):SL1-SL20.

   doi: 10.1190/INT-2014-0033.1

6. Vermeer GJO. Creating image gathers in the absence of proper common-offset gathers. *Explor Geophys*. 1998;29(3-4):636-642.

   doi: 10.1071/EG998636

7. Duan W, Xie H, Cui Y. Full Azimuth Tomography Velocity Modeling and Depth Imaging in OVT Domain: Case Study of HQ Full Azimuth Survey in Tarim Basin. In: Schneider RV, ed. *International Meeting for Applied Geoscience & Energy*. Vol 1. Society of Exploration Geophysicists; 2015:5300-5304.

   doi: 10.1190/segam2015-5793166.1

8. Tarantola A. Inversion of seismic reflection data in the acoustic approximation. *Geophysics*. 1984;49(8):1259-1266.

   doi: 10.1190/1.1441754

9. Virieux J, Operto S. An overview of full-waveform inversion in exploration geophysics. *Geophysics*. 2009;74(6):WCC1-WCC26.

doi: 10.1190/1.3238367

10. Baeten G, de Maag JW, Plessix RE, *et al*. The use of low frequencies in a full-waveform inversion and impedance inversion land seismic case study. *Geophys Prospect*. 2013;61(4):701-711.

doi: 10.1111/1365-2478.12010

11. Wang M, Hu Y, Zhang Z, Shi C, Liao X. Automatic differentiation-based weighted instantaneous phase inversion. *J Seism Explor*. 2026;35(2):025520132.

doi: 10.36922/JSE025520132

12. Lim K, Chung W, Shin J, Ha J. Direct envelope-based reflection full waveform inversion for shallow marine seismic data. *J Seism Explor*. 2026;35(2):026030005.

doi: 10.36922/JSE026030005

13. Adwani A, Danilouchkine M, Al-Siyabi Q, *et al*. Onshore model building using elastic full-waveform inversion on surface and body waves: A case study from Sultanate of Oman. *Geophysics*. 2022;87(6):R413-R424.

doi: 10.1190/geo2021-0751.1

14. Hu G, Xu W, He B, He W, Du Z, Yao J. DIW-based reflection full waveform inversion and its application of land seismic data. *J Geophys Eng*. 2023;20(6):1109-1116.

doi: 10.1093/jge/gxad070

15. Bunks C, Saleck FM, Zaleski S, Chavent G. Multiscale seismic waveform inversion. *Geophysics*. 1995;60(5):1457-1473.

doi: 10.1190/1.1443880

16. Guitton A. Blocky regularization schemes for full-waveform inversion. *Geophys Prospect*. 2012;60(5):870-884.

doi: 10.1111/j.1365-2478.2012.01025.x

17. Zhang P, Wu RS, Han L, Zhou Y. Strong-scattering multiparameter reconstruction based on elastic direct envelope inversion and full-waveform inversion with anisotropic total variation constraint. *Remote Sens*. 2023;15(3):746.

doi: 10.3390/rs15030746

18. Liu B, Sacchi MD. Minimum weighted norm interpolation of seismic records. *Geophysics*. 2004;69(6):1560-1568.

doi: 10.1190/1.1836829

19. Xu S, Zhang Y, Pham D, Lambare G. Antileakage Fourier transform for seismic data regularization. *Geophysics*. 2005;70(4):V87-V95.

doi: 10.1190/1.1993713

20. Nguyen T, Winnett R. Seismic interpolation by optimally matched Fourier components. In: *2011 SEG Annual Meeting*. Society of Exploration Geophysicists; 2011. https://onepetro.org/SEGAM/proceedings-abstract/SEG11/SEG11/SEG-2011-3085/97479

21. Schonewille MA, Yan Z, Bayly MP, Bisley R. Matching Pursuit Fourier Interpolation Using Priors Derived from a Second Data Set. In: *Proceedings*. EAGE Publications BV; 2013.

doi: 10.3997/2214-4609.20130384

22. Sun M, Zhang J, Zhang W. Alternating first-arrival traveltime tomography and waveform inversion for near-surface imaging. *Geophysics*. 2017;82(4):R245-R257.

doi: 10.1190/geo2016-0576.1

23. Lailly P. The Seismic Inverse Problem as a Sequence of Before Stack Migrations. In: Bednar JB, Robinson E, Weglein AR, editors. *Conference on Inverse Scattering-Theory and Application*. SIAM; 1983. p. 206-220.

24. Sirgue L, Pratt RG. Efficient waveform inversion and imaging: A strategy for selecting temporal frequencies. *Geophysics*. 2004;69(1):231-248.

doi: 10.1190/1.1649391

25. Rickett J. The variable projection method for waveform inversion with an unknown source function. *Geophys Prospect*. 2013;61(4):874-881.

doi: 10.1111/1365-2478.12008